The Role of Solvent Molecular Weight in Shear Thickening and Shear Jamming

SCHOLARONE™
Manuscripts

Soft Matter

The Role of Solvent Molecular Weight in Shear Thickening and Shear Jamming

Mike van der Naald,$^{*a\ b}$ Liang Zhao,^{ab}, Grayson L. Jackson^{a} and Heinrich M. Jaeger^{ab}

The application of stress can drive a dense suspension into a regime of highly non-Newtonian response, characterized by discontinuous shear thickening (DST) and potentially shear jamming (SJ), due to the formation of a frictionally stabilized contact network. Investigating how the molecular weight of the suspending solvent affects the frictional particle-particle interactions, we report on experiments with suspensions of fumed silica particles in polyethylene glycol (PEG). Focusing on the monomer-to-oligomer limit, with $n = 1$ to 8 ethylene oxide repeat units, we find that increasing n enhances shear thickening under steady-state shear and even elicits rapidly propagating shear jamming fronts, as assessed by high-speed ultrasound imaging of impact experiments. We associate this behavior with a weakening of the solvation layers surrounding the particles as n is increased, which thereby facilitates the formation of frictional contacts. We argue that for n larger than the monomer-to-oligomer limit the trend reverses and frictional interactions are diminished, as observed in prior experiments. This reversal occurs because the polymeric solvent transitions from being enthalpically bound to entropically bound to the particle surfaces, which strengthens solvation layers.

1   Introduction

Over the past decade, simulations and experiments have shown that discontinuous shear thickening (DST) and shear jamming (SJ) are macroscopic consequences of microscopic stress-activated frictional contacts between particles which constrain their relative motion[1–6]. Initially "lubricated" particle contacts are converted into "frictional" contacts by the mechanical stress applied[7,8]. Increasing the applied stress increases the fraction of frictional contacts and eventually generates "force chains" of particles that underlie dramatic increases in viscosity and jamming behavior[9–11]. Taking cues from dry granular physics, much work has focused on factors that directly modify the frictional properties of surfaces such as changing the sliding friction (or rolling friction) coefficient and related experimental studies which have investigated the effects of particle roughness, size, aspect ratio, or surface chemistry[12–20]. However, the fundamental difference between dry granular media and a suspension is the presence of a suspending liquid, the solvent, which wets and lubricates each particle. The transition to a "frictional" particle contact thus necessarily involves displacement of the intervening solvent and de-solvation of the particle surface. As such, for a given solvent its chemical properties such as molecular weight or pH are important and easily tunable parameters that can affect the nature of

frictional contacts between particles.[21]

Though the role of polymeric solvent molecular weight (MW) in strongly shear-thickening (nearly DST) suspensions has been investigated in several prior studies, the outcome has not been clear. Some of these studies found that increasing the MW diminishes shear thickening[22–24], while others show that it enhances shear thickening instead[25,26]. Specifically, for glass or zirconium dioxide particles in silicone oil, Xu et al. found that increasing the MW of the oil led to a smooth crossover from highly non-Newtonian, essentially DST behavior to completely Newtonian flow[22]. Conversely, studies by Raghavan et al., using fumed silica in polypropylene glycol (PPG), showed that increasing the MW led to more pronounced non-Newtonian behavior, from continuous shear thickening (CST) to nearly DST[26]. These findings indicate some of the complexity associated with the interactions between particle surfaces and the solvent molecules. To gain further insight, we here extend earlier investigations in two ways. First, we focus on the limit of very small MW so that we can track the evolution of suspension behavior as the solvent molecules are increased in chain length from monomers to oligomers. Second, we extend the upper range of applied shear stress in order to go beyond the DST regime and test how SJ is affected by changing the solvent.

Our experiments use fumed silica particles suspended in polyethylene glycol (PEG). Compared to other materials often used in studies of shear thickening that are available in bulk quantities, such as cornstarch, fumed silica has the advantage that DST can be observed at very low packing fractions, due to the particles'

^{a} *James Franck Institute and Department of Physics, University of Chicago, Chicago, Illinois, USA. Tel: 503-704-6106; E-mail: mrv@uchicago.edu*
^{b} *Department of Physics, The University of Chicago, Chicago, Illinois, USA.*
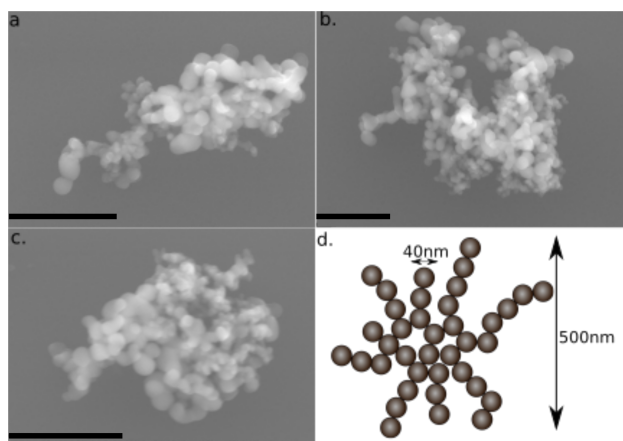
Fig. 1 (a)-(c) Representative SEM micrographs Aerosil OX50 aggregates. Each scale bar is 500nm. d. Schematic illustration of a fumed silica aggregate composed of smaller primary silica particles (40nm) that fused together. The average aggregate is 500nm with a broad size distribution.

highly non-spherical shape. Fumed silica also is non-porous and has a well-controlled surface chemistry. As solvents we use three different molecules of similar chemical structure, but increasing number n of ethylene oxide repeat units: ethylene glycol (EG, $n = 1$), PEG-200 ($n \approx 4$), and PEG-400 ($n \approx 8$). We characterize the steady-state flow behavior of these fumed silica suspensions using a stress-controlled rheometer in parallel plate geometry. At identical volume fractions, we observe the least shear thickening in EG, followed by PEG-200, and the strongest shear thickening in PEG-400. We use high-speed ultrasound imaging to visualize the transient flow fields under impact. While we observe a localized flow field around the impactor typical of a viscous, fluid-like response for EG suspensions, PEG-200 suspensions yield extended, highly correlated motion indicative of a shear jammed solid. This result constitutes the first direct observation of propagating jamming fronts associated with shear jamming in a fumed silica suspension. We then develop a scenario in which we relate the propensity of forming frictional interparticle contacts to the strength of solvation layers surrounding the particles. We use this to explain both the observed enhancement of non-Newtonian stress response for n up to 8 and its demise for larger n.

2 Materials and Methods

2.1 Suspension Preparation

The solid particles used in this study are fumed silica (Aerosil OX50, Evonik) with specific density $\rho = 2.2$g cc^{-1}. They are aggregates of 40 nm glass spheres that irreversibly fused during the manufacturing process to form irregularly shaped particles approximately 500 nm in size.

Representative scanning electron microscope (SEM) pictures of these aggregates are shown in Fig. 1(a-c) while a schematic of the particles is shown in Fig. 1(d). We suspended these particles in ethylene glycol (EG) (Fisher Chemical, MW $= 67.07 \frac{g}{mol}$), PEG-200 (Alpha Aesar, average MW $= 200 \frac{g}{mol}$), and PEG-400 (Sigma-Aldrich, average MW $= 400 \frac{g}{mol}$). These solvents are linear chains

containing n ethylene oxide repeat units. We measured each solvents viscosity η_0 to calculate reduced vicosity of our suspensions, $\eta_R = \frac{\eta}{\eta_0}$, and ensure that each solvent is a Newtonian fluid, as shown in figure S2. For EG, $n = 1$, while on average, PEG-200 has $n = 4$ and PEG-400 has $n = 8$. We needed to make large amounts of suspension (≈ 100 mL) for our impact experiments and smaller amounts (≈ 1 mL) for steady-state rheometry. We found that large quantities required much longer mixing times. For this reason we developed two suspension preparation protocols described below. To determine the packing fraction ϕ_v we weighed both the solvent and solid particles using an analytical balance and converted to volumes fractions using their respective densities. Since our particles are porous amorphous aggregates, some of the suspending liquid is inside the particle and the packing fractions reported here should be regarded as effective packing fractions. For small volumes of suspension (≈ 1 mL), the mixture was stirred manually with a spatula until all dry powder had been mixed in. ***Caution: Dry fumed silica powder is easily fluidized and represents an inhalation hazard.*** Therefore, all handling of fumed silica powder was conducted in a fume hood. Subsequently, large air bubbles were removed by placing the suspension in a centrifuge at 1000 rpm for 1 minute. The samples were then placed in a water bath sonicator at 40 kHz and 130 W for six hours. These lengthy mixing and sonication times were necessary to ensure that micron-scale agglomerates of particles were broken up and individual particle aggregates (Fig. 1) were well-dispersed, a key requirement for reproducible rheometry.

For large amounts of suspension (≈ 100 mL), the particle-fluid mixture was stirred using an overhead mixer in a fume hood at 200 rpm until there was no more visible dry powder, usually taking two hours. Mixing for extended periods of time at such high rotation rates introduced large air bubbles into the suspension. These were especially problematic in impact experiments, as they strongly scatter sound waves and significantly limit ultrasound imaging quality. In order to debubble our suspension, we sealed it and placed it on a 3Hz linear shaker for five hours. This removed all of the large air bubbles but left a number of evenly distributed very small air bubbles, which then served as tracers during ultrasound imaging.

2.2 Steady State Rheology

Steady-state shear experiments used a stress-controlled Anton Paar MCR301 rheometer with a parallel plate (25mm in diameter) geometry. All experiments were performed within a temperature range of 22-25 °°C and all runs were conducted less than one hour after sonication. The gap size between the parallel plates was set as needed, but kept between 0.1-0.2 mm, which we found helped in accessing higher stresses without sample ejection. Before measurements we applied a pre-shear at constant shear rate $50 \frac{1}{s}$ for 200 s to a produce homogeneous starting condition for all samples. To check for wall slip, we measured our highest packing fractions in PEG-200 and PEG-400 in a 25mm parallel plate geometry at two different gap heights, 25mm parallel plate geometry with roughened top and bottom plates at two different gap heights, and a 25mm cone and plate geometry with
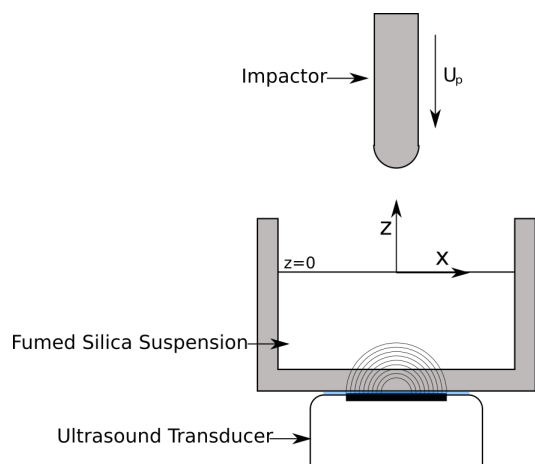
Fig. 2 Schematic of the impact experiments. The suspension is placed in a cylindrical container of diameter 5.0 cm and impacted with a rod that has a hemispherical cap of diameter 1.0 cm. Once the impactor approaches the suspension surface, ultrasound imaging at 4,000 frames per second is triggered and provides a video of a slice of the flow-field in the *x-z* plane.

roughened top and bottom plates shown in Figure. S1. While there was some deviation between the different geometries, this is mainly in the low stress behavior which we found to be dependent on how the plates were roughened, the gap size, and whether we imposed a constant stress or constant rate. This indicates that the low stress behavior in these systems is delicate and requires future study but the enhancement of shear thickening with increasing MW is independent of measurement geometry or boundary roughness. Note that, despite the high shear rates used in our measurement, the high viscosity of the suspending liquid ensures that we are operating well below the regime where secondary flows emerge. Additionally, the highest particle Reynold's number reached was 0.00005 ≪ 1, meaning that particle inertia can safely be neglected. We checked for edge fracture in all of our samples using a high speed video camera (Phantom v12) equipped with a 200 *mm* lens to observe the sample edge during our rheological measurements. We did not observe edge fracture as observed in polymeric systems[27] but instead observed portions of the suspension-air interface change in reflectivity and surface texture, as also previously observed by video in suspensions in the DST regime just before jamming[28,29].

2.3 Impact Experiments

To study the transient behavior, we used high-speed ultrasound imaging to track the flow field inside the suspension under impact[6,30–32]. The setup is illustrated in Fig. 2. The suspension was placed in a 3D-printed cylindrical container with an inner diameter of 5 cm. An impactor driven at adjustable speed U_p by a linear actuator (SCN5, Dyadic Systems) was mounted above the container. The impactor employed a cylindrical rod with a hemispherical cap of diameter 1 cm. An ultrasound transducer (Philips L7-4) was placed under the bottom of the container, coupled acoustically through a layer of ultrasound gel. This transducer consisted of a linear array of 128 piezoelectric elements

and was aligned along the *x* direction.

In the experiments reported here, the rod moved vertically downward along the central axis of the container at constant speed $U_p = 300\frac{mm}{s}$ and impacted the suspension directly above the transducer. Ultrasound imaging was triggered to begin when the rod reached a position 1 mm above the surface of the suspension and collected 500 consecutive frames at a rate of $4000s^{-1}$. The impactor pushed vertically 15 mm deep into the suspension, so that it stopped before the ultrasound imaging ended . The images are 2D slices in the *x-z* plane under the rod, as displayed in Fig. 2. Impact experiment was repeated nine to fifteen times for each suspension, and the resulting flow fields, extracted from particle image velocimetry (PIV), were averaged. After each impact, the suspension was fully relaxed by stirring with a spatula as well as by gently shaking and rotating the container.

3 Results

3.1 Steady State Rheology

In Fig. 3a and 3b we plot the flow curves for four different packing fractions ϕ_v, reported as shear stress σ, versus reduced viscosity $\eta_R = \frac{\eta}{\eta_0}$ for both PEG-200 and EG. Here η_0 is the viscosity of the suspending solvent. The upper limit in each case was chosen such that we could measure the greatest extent of thickening without sample ejection or free surface deformation during or after each test. All curves in Fig. 3 are an average of two forward and backwards ramps; that they all lay approximately on top of each other indicates that we were sampling the steady state viscosity. Error bars are calculated from the standard deviation in the forward and backward ramp and are on the order of the marker size.

All suspensions show shear thinning at low stresses followed by a minimum in the viscosity and subsequent shear-thickening beyond an onset stress (τ_c). From Fig. 3a and Fig. 3b we see that increasing the packing fraction in PEG-200 enhances both the shear thinning and the degree of thickening, while increasing the packing fraction in EG only enhances the degree of thickening. Comparison between similar packing fractions from Fig. 3a and Fig. 3b indicates markedly different slopes for the shear thickening as a function of solvent MW. Flow curves that only show mild CST in EG (slope 0.44 on a log-log plot of viscosity as a function of shear stress) now exhibit clear DST in PEG-200 (slope 1). Associated with this change in the thickening behavior in going from EG to PEG-200, we find an increase in the shear thinning, and the minimum in viscosity shifts from a stress of $\tau_c = 11$Pa in EG to a stress of $\tau_c = 100$Pa in PEG-200. To further highlight the role of solvent MW we directly compare suspensions at similar particle concentration $\phi_v \approx 0.33$ but different solvent. This is shown in Fig. 3c as a function of stress and in Fig. 3d as a function of rate.

3.2 Transient Dynamics

To analyze the flow fields of the suspensions under impact, we used a particle imaging velocimetry (PIV) algorithm to extract local velocities $\mathbf{v} = (v_x, v_z)$ from the displacement of tiny air bubbles between successive ultrasound images. Because of the cylindrical symmetry in our system, these two velocity components suffice
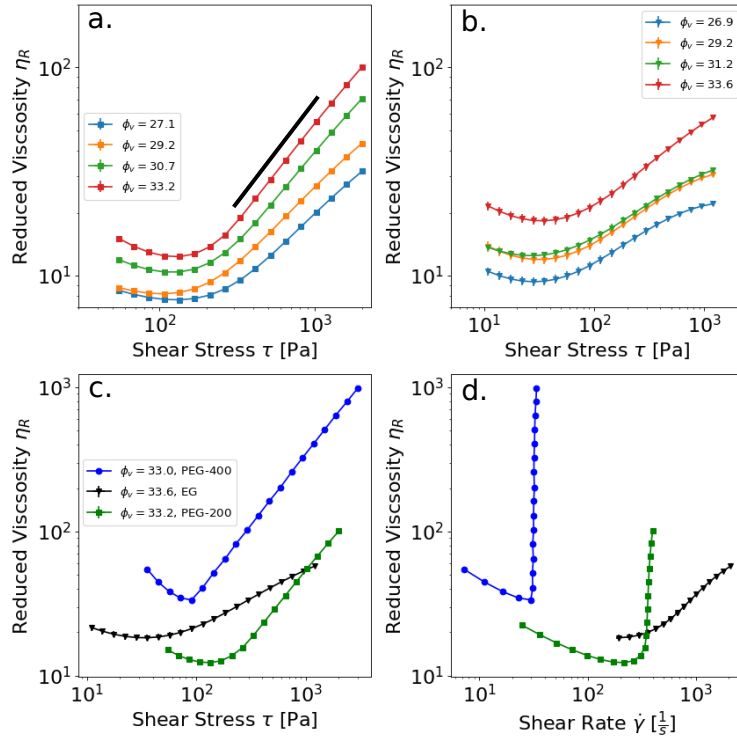
Fig. 3 Steady state rheometry data from suspensions of Aerosil OX-50 particles. Viscosity is plotted as a function of shear stress in PEG-200 (a) and EG (b). The black line in (a) has a slope of 1 indicating that the flow curve corresponding to a packing fraction $\phi_v = .3323$ is undergoing discontinuous shear thickening (DST). Viscosity curves for solvents of different MW but similar packing fraction are plotted as a function of shear stress (c) and shear rate (d).

to reconstruct the entire 3D flow field[31]. The impactor hit the suspension surface $z = 0$ mm at $t = 0$ s and continued to move downwards at $U_p = 300 \frac{mm}{s}$ into the suspension. Figure. 4 shows how the flow fields evolve with time after this impact for suspensions of $\phi_v \approx 0.33$ in PEG-200, one suspended in PEG-200 and the other in EG. The colormap shows the value of v_z, the velocity component in the z direction.

Here we first consider the suspension in EG, shown in the top row of Fig. 4. In all three time frames, the flow is highly localized within one centimeter around the impactor tip. This highly dissipative response is what one expects from a viscous liquid. In contrast, we observe a dramatically different response in PEG-200, shown in the bottom row of Fig. 4. We see a large region, shown as the bright area, which expands into the bulk of the material in both longitudinal and transverse directions. This bright area exhibits a large downward velocity but small internal velocity gradient, as expected for a solid-like state, while the dark region ahead of it is still quiescent. This indicates a large local shear rate at the leading edge of the solid-like region, which is the signature of a shear jamming front, as previously discovered in cornstarch suspensions at much higher packing fraction[31].

To more quantitatively prove that the jamming front forms only in the PEG-200 suspension, we calculate the spatial shear rate distribution. The strain rate tensor in a rotational symmetric system is given by[32]

$$\underline{\underline{\dot{\varepsilon}}} = \begin{bmatrix} \frac{\partial v_r}{\partial r} & 0 & \frac{1}{2}(\frac{\partial v_r}{\partial z} + \frac{\partial v_z}{\partial r}) \\ 0 & \frac{v_r}{r} & 0 \\ \frac{1}{2}(\frac{\partial v_r}{\partial z} + \frac{\partial v_z}{\partial r}) & 0 & \frac{\partial v_z}{\partial z} \end{bmatrix}. \quad (1)$$

We can express the effective magnitude of local shear by a strain rate scalar

$$\dot{E} = \sqrt{(\lambda_1^2 + \lambda_2^2 + \lambda_3^2)/2}, \quad (2)$$

where λ_1, λ_2, and λ_3 are the eigenvalues of $\underline{\underline{\dot{\varepsilon}}}$ in Eq. (1). $\dot{E}$ for the $\phi_v \approx 0.33$ OX50-EG suspension at three time frames is shown in Fig. 5 (a)-(c). We see that the distance between the rod tip and the $v_z = 0.5U_p$ isocontour remains constant during the whole impact process. Also, the region with maximum $\dot{E}$ is concentrated immediately next to the rod. Taken together, this reveals that the OX50-EG suspension under impact does not jam into a solid-like region with a propagating leading edge (jamming front), but remains a viscous fluid.

The bottom row of Fig. 5 shows $\dot{E}$ for the same three time frames when the solvent is switched to PEG-200. Behind the shear jamming front, the dark blue region indicates a low shear rate, which corresponds to a solid-like region continuously propagating and expanding into the suspension. $\dot{E}$ peaks in the shell-like region close to the isocontour $v_z = 0.5U_p$ for all time frames, while it is almost invariant along this shell. This coincides with the rapid decrease in velocity at the boundary between the jamming front and the unjammed, still liquid-like suspension ahead of it.
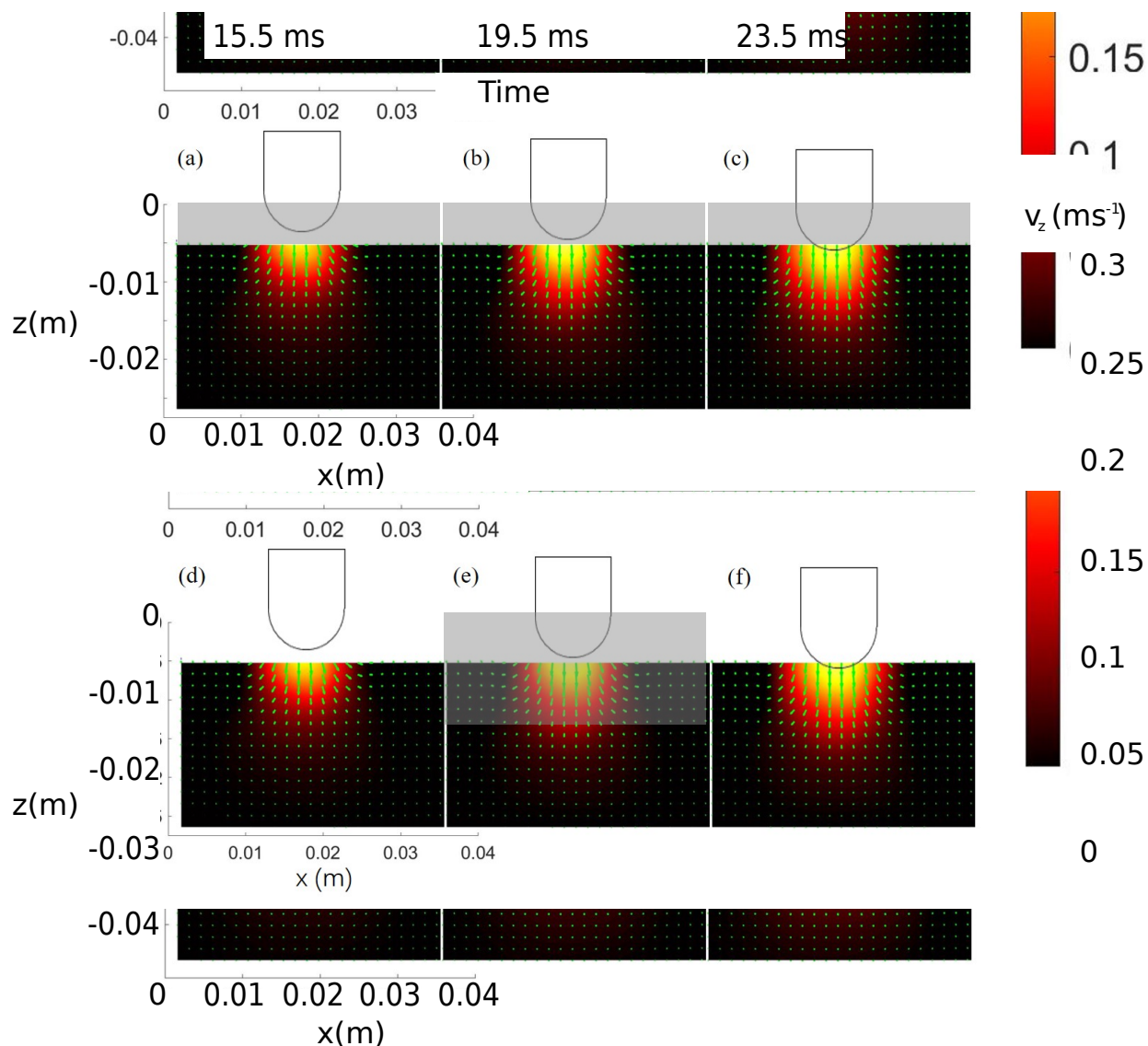
Fig. 4 Velocity fields and v_z isocontours for impact into Aerosil OX50 suspensions with $\phi_v \approx 0.33$. Shown are snapshots at times $t = 15.5$ ms (a,d), $t = 19.5$ ms (b,e), and $t = 23.5$ ms (c,f) after the impactor reached the suspension surface. Two different solvents are used. The top row (a)-(c) shows results for EG and the bottom row (d)-(f) for PEG-200. Suspension surfaces are at $z = 0$ m and the container bottoms are at $z = -0.03$ m and $z = -0.045$ m for the top and bottom row, respectively. Small green arrows indicate local velocities v_x and v_z. The color mapping tracks v_z, with the upper limit (white) corresponding to the impactor speed ($U_\mathbf{p}$). The actual positions of the impactor in each time frame are outlined. The grey regions indicate the remaining height of the suspension from the field of view of the ultrasound images to the top surface of the suspension.
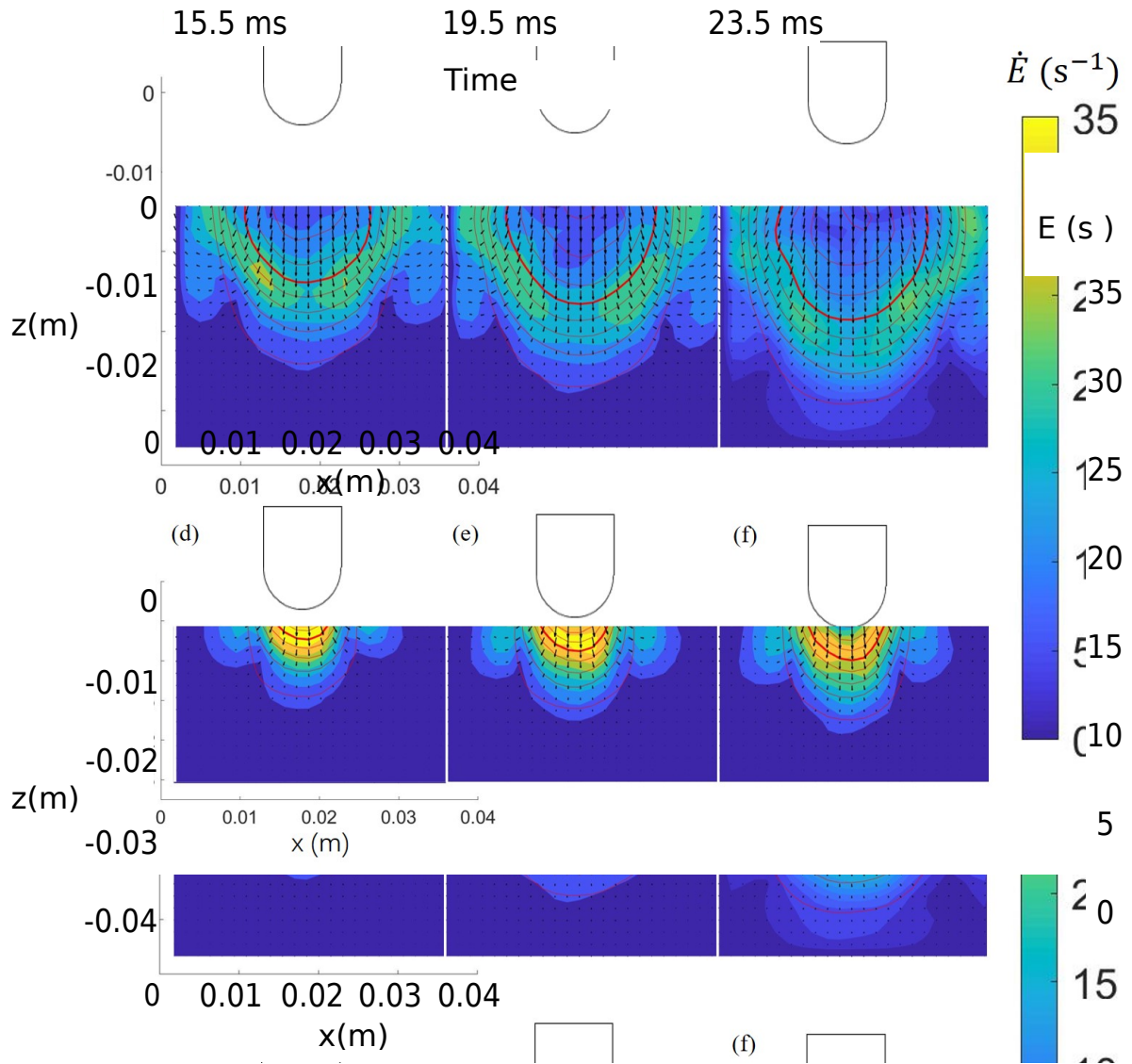
Fig. 5 Local shear intensity expressed by the strain rate scalar $\dot{E}$ at times $t = 15.5\text{ms}$ (a, d), $t = 19.5\text{ms}$ (b, e), and $t = 23.5\text{ms}$ (c, f) after the impactor reached the surface of the suspension. The suspensions are the same as in Fig. 4: Aerosil in EG (top row) and PEG (bottom row). The color map corresponds to the value of $\dot{E}$. Red curves show the isocontours of v_z from $v_z = 0.1U_p$ to $v_z = 0.9U_p$, with increments of $0.1U_p$. The thick curves show $v_z = 0.5U_p$, which we define as the locus of the jamming fronts. The grey region indicates the remaining height of the suspension from the field of view of the ultrasound images to the free top surface.
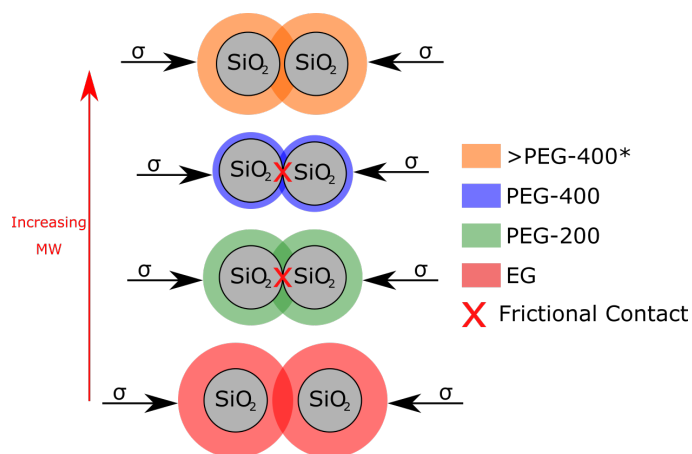
Fig. 6 Schematic depiction of solvation layers that resist the formation of frictional interparticle contacts and that change as a function of increasing solvent molecular weight. Shaded regions in orange, blue, green, and red surrounding the particles depict the solvation layer of strongly bound solvent molecules. For EG the solvation layer is strong and the applied stress cannot overcome the energetic penalty for desolvation. But in both PEG-200 and PEG-400 the solvation layer is relatively weak, so an applied stress σ can give rise to frictional contacts. *We conjecture that if we could measure fumed silica suspensions in higher MW PEG's (higher MW PEG's are solid at room temperature) that this trend of decreasing solvation layer strength would eventually reverse and the stress required to form frictional contacts would start to increase.

3.3 Discussion

Many studies have demonstrated that the dramatic increases in viscosity associated with DST and the solid-like behavior seen in SJ result from the formation of frictionally-stabilized, percolating contact networks [3,5,9,20,33–35]. However, these frictional contacts can only form once the applied stress overcomes the repulsive barriers associated with surface solvation (i.e. lubrication breakdown). The data reported here for fumed silica demonstrate that increasing the MW of the suspending solvent elicits DST in PEG-200 at packing fractions that exhibit only CST in EG. Furthermore, in PEG-200 at concentrations far below those required with cornstarch, the suspensions show solid-like, shear jammed behavior under impact, while in EG they behave like viscous fluids. Increasing the MW further by going to PEG-400 only enhances shear thickening. The dramatically different stress responses indicate that even subtle changes in solvent MW affect the ability of the force chain network to resist applied shear.

This effect could be due to either changes in the effective friction coefficient (μ_{eff}) between particle surfaces or changes in the stress-dependent balance of lubricated to frictional contacts. However, as the particle surface chemistry is the same in all suspensions studied here, the friction coefficient between desolvated surfaces is likely identical. This reasoning implies that the solvent MW tunes the repulsive force profile between approaching silica surfaces responsible for resisting frictional interparticle contacts. This scenario whereby weakening the repulsive barrier between particles leads to more particles interacting frictionally and thus enhanced shear thickening has recently been suggested to explain similar results in suspensions with polymer additives [36].

The scenario we are proposing, therefore, is that an increase in the solvent MW decreases the strength of the surface solvation layer and enables particles to enter into frictional contact at lower applied stresses (Fig. 6). In other words, the force profile between silica surfaces in PEG-200 is less repulsive than in EG. Thus, a greater applied stress is required to force particles into frictional contact in EG. Our reasoning is consistent with measurements of the second virial coefficient for dilute samples of 40nm silica dispersed in polyethylene glycol melts [37]. Anderson and Zukoski observed a highly repulsive interaction between silica particles in EG, whereas the interparticle potential in PEG-400 and longer PEGs is only slightly more repulsive than their hard-sphere equivalents. While we are unaware of studies in higher MW PEG, atomic force microscopy (AFM) measurements similarly reported a steep and long-ranged repulsive force that extends over 5 nm between silica surfaces in EG [38]. These literature precedents coupled with our rheological and impact experiments suggest that the force required to make frictional contacts decreases with increasing MW (Fig. 6).

While not the focus of this study, we note that the enhanced shear thinning behavior at low applied stress or shear rate as we move from EG to PEG-400 signals an increase in long-ranged attractive forces between particles [39]. As a result of the enhanced shear thinning, also the characteristic stress τ_c associated with the minimum of the viscosity curve $\eta_r(\tau)$ moves to larger values (see Fig. 3c). While this minimum stress is sometimes identified with the onset of shear thickening, i.e., with the critical stress required to push particles into frictional contact, we caution against this interpretation since the true onset stress is likely obscured by the strong shear thinning in all samples, as has been noted in other studies [39,40].

We now turn our attention to the specific molecular mechanisms that underlie the relative solvent layer strengths. The adhesion energy and resulting conformation of polymer chains at particle surfaces is well known to influence the macroscopic properties of composite materials [41–43]. Polyethylene glycol chains primarily interact with surface silanol (Si-OH) groups through hydrogen bonds with backbone ether (-O-) or terminal hydroxyl (-OH) groups. The hydroxyl end groups have a much larger binding affinity for the silica surface than the ether oxygens [41–43]. As the MW increases, the concentration of hydroxyl end groups decreases and results in a less strongly bound surface solvation layer. Furthermore, increasing polymer MW results in less dense surface layers by virtue of their less compact conformation at the particle surface [42,44,45]. The solvation layer in EG is thus denser and also has a larger enthalpic cost for desolvation. Furthermore, solvation of the silica surface by EG facilitates silanol group dissociation (Si-OH $\rightarrow$ Si-O$^-$ + H$^+$) [37]. In summary, consistent with arguments by Raghevan, Walls and Khan [26], the increased hydrogen bonding between particle and solvent leads to a stronger, enthalpically stabilized surface solvation layer in EG that stabilizes the dispersed or "lubricated" state. Increasing the MW decreases this barrier and facilitates frictional interparticle interactions at lower applied stresses. To be sure this phenomena is driven mainly by solvation forces we can follow Raghevan, Walls and Khan [26] and estimate the van der Waal's forces between the particles in the three sus-

pending solvents. Using index of refractions and dielectric constants from the literature [46] we find that the van der Waal's forces for particles in PEG-200 and PEG-400 nearly vanish while for EG there is a small repulsion that contributes to the particles having the largest barrier to frictional contacts in EG.

Our current results and interpretation differ from a number of other studies [22–25], which concluded that increasing solvent MW suppresses shear thickening due to a more strongly adsorbed surface polymer layer. However, these other studies did not investigate the low MW regime of monomer to oligomer and only investigated polymers with 7 or more repeat units. Surprisingly, even increasing the degree of polymerization of polypropylene glycol (PPG) from $n=7$ to 17 already shows a (small) decrease in shear thickening [24,26]. In this slightly higher MW regime, a number of studies demonstrated that overall surface coverage increases with MW [42,47,48]. In other words, the multidentate binding with increasing MW beyond a certain limiting value of n (perhaps around 8-10 in our case) leads to a reduced translational entropy cost for each subsequent binding event and leads to a higher binding coefficient per polymer segment. This entropically bound polymer layer could then lead to a steric barrier that inhibits frictional particle contacts, which could explain the decreased shear thickening and shift towards higher τ_c with higher MW reported by Shenoy and Wagner [23]. Alternatively, as Xu et al. [22] observed no change in τ_c but decreased shear thickening with increasing MW, the bound polymer layer could simply "cap" surface hydroxyl groups and lead to a lower effective interparticle friction coefficient. Thus, beyond a certain characteristic MW the trend can reverse and frictional interactions start to diminish (Fig. 6, top row). Where this cross-over takes place is likely to depend on details of the particle surfaces. For example, if the very rough fumed silica agglomerates are replaced by comparatively smooth silica spheres, this cross-over might shift to slightly lower n. Indeed, we find a similar increase in shear thickening strength when switching from EG to PEG-200, but for PEG-400 there is already an indication that the maximum in frictional interaction has been exceeded as shown in Fig. S3

4   Conclusion

The rheological response of shear thickening fluids is a consequence of microscopic interactions. As such, macroscopic changes in the flow profiles are in fact a sensitive reporter of subtle changes in molecular-level interactions. In this study, we investigated the effect of PEG MW on the shear thickening behavior of fumed silica suspensions. By steady-state rheology, we observed that increasing PEG MW led to increased shear thickening. Similarly, by high-speed ultrasound imaging, we observed, for the first time directly, how increasing the MW elicits SJ under impact. We find that the extent of shear thickening and the ability to enter the SJ state are highly dependent on the choice of suspending solvent, which we interpret in light of the stress-dependent balance of lubricated versus frictional contacts. On the basis of prior adsorption and AFM studies we argue that increasing the number of polymer solvent repeat units, n, up to a certain characteristic value weakens the solvation layer surrounding the particles by decreasing the density of more strongly binding -OH end groups.

This weakening of the solvation layer lowers the stress required to push particles into frictional contact which is ultimately responsible for the increase in shear thickening. While PEG solvents with higher MW, i.e., larger n, are solid under our experimental conditions, comparisons with literature precedents of analogous PPG suspensions [24,26] suggest that even slightly increasing the PEG MW further would actually suppress shear thickening as the system crosses over from a regime where solvation layers are enthalpically-stabilized at low MW ($\leq 400 \frac{g}{mole}$ for PEG) to one where they are entropically-bound at higher MW. As a consequence of such crossover, shear thickening may in fact be most pronounced at some intermediate MW. This crossover resolves the apparent contradiction between our current results and previous studies [22–24] as those studies investigated the higher MW regime where polymers are entropically bound to the particle surface.

Taken together, these findings also open up new opportunities to control both shear thickening and shear jamming in industrial settings, as changing the relative surface affinity of the solvent is much easier than modifying particle properties such as size, shape, or surface chemistry. Our results show that shear jamming during suspension processing can be suppressed (or enhanced) through judicious selection of a solvent that will strongly (or weakly) solvate particle surface chemical functionalities and therefore inhibit (or facilitate) frictional interparticle contacts.

Conflicts of interest

There are no conflicts of interest to declare.

Acknowledgements

Notes and references

1 M. Hermes, B. M. Guy, W. C. K. Poon, G. Poy, M. E. Cates and M. Wyart, *J. Rheol.*, 2016, **60**, 905–916.

2 A. Singh, R. Mari, M. M. Denn and J. F. Morris, *J. Rheol.*, 2018, **62**, 457–468.

3 N. Fernandez, R. Mani, D. Rinaldi, D. Kadau, M. Mosquet, H. Lombois-Burger, J. Cayer-Barrioz, H. J. Herrmann, N. D. Spencer and L. Isa, *Phys. Rev. Lett.*, 2013, **111**, 108301.

4 R. Mari, R. Seto, J. F. Morris and M. M. Denn, *Proc. Natl. Acad. Sci. U.S.A*, 2015, **112**, 15326–15330.

5 J. R. Royer, D. L. Blair and S. D. Hudson, *Phys. Rev. Lett.*, 2016, **116**, 188301.

6 S. Majumdar, I. R. Peters, E. Han and H. M. Jaeger, *Phys. Rev. E*, 2017, **95**, 012603.

7 N. Y. C. Lin, B. M. Guy, M. Hermes, C. Ness, J. Sun, W. C. K. Poon and I. Cohen, *Phys. Rev. Lett.*, 2015, **115**, 228304.

8 J. F. Morris, *Phys. Rev. Fluids*, 2018, **3**, 110508.

9 R. Mari, R. Seto, J. F. Morris and M. M. Denn, *J. Rheol.*, 2014, **58**, 1693–1724.

10 R. Radhakrishnan, J. R. Royer, W. C. K. Poon and J. Sun, *Gran. Matt.*, 2020, **22**,.

11 R. Mari and R. Seto, *Soft Matter*, 2019, **15**, 6650–6659.

12 A. Singh, C. Ness, R. Seto, J. J. de Pablo and H. M. Jaeger, *Phys. Rev. Lett.*, 2020, **124**, 248005.

13 N. M. James, E. Han, R. A. L. de la Cruz, J. Jureller and H. M. Jaeger, *Nat. Mater.*, 2018, **17**, 965–970.

14 N. M. James, C.-P. Hsu, N. D. Spencer, H. M. Jaeger and L. Isa, *J. Phys. Chem. Lett.*, 2019, **10**, 1663–1668.

15 I. Buttinoni, J. Cha, W.-H. Lin, S. Job, C. Daraio and L. Isa, *Proc. Natl. Acad. Sci. U.S.A*, 2017, **114**, 12150–12155.

16 N. M. James, H. Xue, M. Goyal and H. M. Jaeger, *Soft Matter*, 2019, **15**, 3649–3654.

17 W. Yang, W. Yang, X. Pei, F. Zhou and Q. Xue, *Langmuir*, 2017, **33**, 1037–1042.

18 P. Bourrianne, V. Niggel, G. Polly, T. Divoux and G. H. McKinley, *arXiv preprint arXiv:2001.02290*, 2020.

19 H. Nakamura, S. Makino and M. Ishii, *The Society of Rheology, Japan*, 2019, **47**, 9–15.

20 B. M. Guy, M. Hermes and W. C. K. Poon, *Phys. Rev. Lett.*, 2015, **115**, 088304.

21 H. M. Laun, *Angew. Makromol. Chem.*, 1984, **123**, 335–359.

22 Q. Xu, A. Singh and H. M. Jaeger, *J. Rheol.*, 2020, **64**, 321–328.

23 S. S. Shenoy and N. J. Wagner, *Rheologica Acta*, 2005, **44**, 360–371.

24 Q. Zhang, C. Wu, Y. Song and Q. Zheng, *Polymer*, 2018, **148**, 400–406.

25 T. Jiang and C. F. Zukoski, *Macromolecules*, 2012, **45**, 9791–9803.

26 S. R. Raghavan, H. J. Walls and S. A. Khan, *Langmuir*, 2000, **16**, 7920–7930.

27 M. Keentok and S.-C. Xue, *Rheological Acta*, 1999, **38**, 321–348.

28 R. Maharjan, E. O'Reilly, T. Postigilione, N. Klimenko and E. Brown, *arXiv preprint arXiv:1606.07650*, 2020.

29 E. Brown and H. M. Jaeger, *Journal of Rheology*, 2012, **56**, 875.

30 E. Han, M. Wyart, I. R. Peters and H. M. Jaeger, *Phys. Rev. Fluids*, 2018, **3**, 073301.

31 E. Han, I. R. Peters and H. M. Jaeger, *Nat. Commun.*, 2016, **7**, 12243.

32 E. Han, L. Zhao, N. Van Ha, T. Hsieh, D. B. Szyld and H. M. Jaeger, *Phys. Rev. Fluids*, 2019, **4**, 063304.

33 R. Seto, R. Mari, J. F. Morris and M. M. Denn, *Phys. Rev. Lett.*, 2013, **111**, 218301.

34 M. Wyart and M. E. Cates, *Phys. Rev. Lett.*, 2014, **112**, 098302.

35 C. Ness and J. Sun, *Soft Matter*, 2016, **12**, 914–924.

36 N. Park, V. Rathee, D. L. Blair and D. Conrad, *Phys. Rev. Lett.*, 2019, **122**, 228003.

37 B. J. Anderson and C. F. Zukoski, *Macromolecules*, 2007, **40**, 5133–5140.

38 D. T. Atkins and B. W. Ninham, *Colloids and Surfaces A*, 1997, **129-130**, 23–32.

39 A. Singh, S. Pednekar, J. Chun, M. M. Denn and J. F. Morris, *Phys. Rev. Lett.*, 2019, **122**, 098004.

40 E. Brown, N. A. Forman, C. S. Orellana, H. Zhang, B. W. Maynor, D. E. Betts, J. M. DeSimone and H. M. Jaeger, *Nat. Mater.*, 2010, **9**, 220–224.

41 S. K. Pattanayek and V. A. Juvekar, *Macromolecules*, 2002, **35**, 9574–9585.

42 P. Trens and R. Denoyel, *Langmuir*, 1993, **9**, 519–522.

43 D. Barbier, D. Brown, A.-C. Grillet and S. Neyertz, *Macromolecules*, 2004, **37**, 4695–4710.

44 S. Cheng, A. P. Holt, H. Wang, F. Fan, V. Bocharova, H. Martin, T. Etampawala, B. T. White, T. Saito, N.-G. Kang, M. D. Dadmun, J. W. Mays and A. P. Sokolov, *Phys. Rev. Lett.*, 2016, **116**, 038302.

45 D. N. Voylov, A. P. Holt, B. Doughty, V. Bocharova, H. M. Meyer, S. Cheng, H. Martin, M. Dadmun, A. Kisliuk and A. P. Sokolov, *ACS Macro Lett.*, 2017, **6**, 68–72.

46 R. Sengwa, K. Kaur and R. Chaudhary, *Polmer International*, 2000, **49**, 599–608.

47 Z. Fu and M. M. Santore, *Macromolecules*, 1998, **31**, 7014–7022.

48 J. M. H. M. Scheutijens and G. J. Fleer, *J. Phys. Chem.*, 1979, **83**, 1619–1635.